NASA-CR-202195

Numerical Modeling of Coronal Mass Ejections

Based on Various Pre-Event Model Atmospheres

by

$A.H.Wang^1, \quad S.T.Wu^1, \quad S.T.Suess^2 \quad and \quad G.Poletto^3$

1. Center for Space Plasma and Aeronomic Research, University of Alabama in Huntsville

2. Space Science Laboratory, NASA/MSFC

3. Observatorie Astrofisico di Arcetri, Florence, Italy

1

Abstract

We examine how the initial state (pre-event corona) affects the numerical MHD simulation for a coronal mass ejection (CME). Earlier simulations based on a pre-event corona with a homogeneous density and temperature distribution at lower boundary (i.e. solar surface) have been used to analyze the role of streamer properties in determining the characteristics of loop-like transients. The present paper extends these studies to show how a broader class of global coronal properties leads not only to different types of CMEs, but also modifies the adjacent quiet corona and/or coronal holes.

We consider four pre-event coronal cases: (1) Constant boundary conditions and a polytropic gas with $\gamma=1.05$; (2) Non-constant (latitude dependent) boundary conditions and a polytropic gas with $\gamma=1.05.$; (3) Constant boundary conditions with a volumetric energy source and $\gamma=1.67$; (4) Non-constant (latitude dependent) boundary conditions with a volumetric energy source and $\gamma=1.67$. In all models, the pre-event magnetic fields separate the corona into closed field regions(streamers) and open field regions. The CME's initiation is simulated by introducing at the base of the corona, within the streamer region, a standard pressure pulse and velocity change. Boundary values are determined using MHD characteristic theory.

The simulations show how different CMEs, including loop-like transients, clouds and bright rays, might occur. There are significant new features in comparison to published results. We conclude that the pre-event corona is a crucial factor in dictating CMEs properties.

Key Words : Sun-Corona, MHD, CME

1. Introduction

Coronal mass ejections (CMEs) are recognized as an important component of the large-scale evolution of the solar corona and as a key factor in the generation of geomagnetic storms. They were first observed with the Orbiting Solar Observatory (OSO-7) white-light coronagraph (Tousey, 1973). Later the Skylab coronagraph, operating during 1973-1974, recorded 77 events (Munro et al., 1979). and the Solwind coronagraph on the P-78 satellite, during 1979-1985, recorded in excess of 1200 events of this kind (Sheeley et al., 1980).

CMEs are observed to occur in a wide variety of sizes and shapes and at various latitudes (Munro et al., 1979; Howard et al., 1984). Munro (1977) has classified the appearance of mass ejection transients observed during the Skylab period; the most dominant type is the outwardly expanding loop, or loops. Clouds or amorphous blobs constitute the next most common type. The remainder defy specific classification. Burkepile and St.Cyr (1993) gave more detail description of apparent morphologies of CMEs. They emphasize that features often do not fall neatly into one category and the shapes of observed features may evolve as they move outward through the corona or may be altered due to projection effects if they move out of the plane of the sky. Typical characteristics of loop transients have been given by Sime et al. (1984).

In CME speed surveys the outward speeds of mass ejection are from less than 100 kms^{-1} to greater than 1200 kms^{-1} at 1.75 and 6 $R_{\odot}$, respectively (Rust et al., 1979; Gosling et al., 1976; Hildner, 1977; Hundhausen et al., 1977). Recently Hundhausen et al. (1994) showed that the average CME speed variation over solar cycle 21 could be a factor three. This average is low in 1984 (157 kms^{-1}), and 1987 (262 kms^{-1}), and high in 1980 (355 kms^{-1}), 1985 (458 kms^{-1}), 1986 (371 kms^{-1}), and 1989 (410 kms^{-1}).

In order to give a physical interpretation of observed coronal mass ejections, numerical magnetohydrodynamic models have been developed, starting in the late 1970s, first in

3

one and then in two dimensions (Dryer et al., 1979; Nakagawa et al., 1976, 1978, 1981; Steinolfson et al., 1982; Steinolfson and Hundhausen, 1989; Wu et al., 1978, 1981, 1982, 1983). In these models, the initial conditions, i.e. the pre-event coronae, vary widely. In the early models, the pre-event corona was assumed to be a hydrostatic, isothermal atmosphere with a magnetic configuration represented either by a dipole potential magnetic field (Dryer et al., 1979; Nakagawa et al., 1976, 1978; Wu et al. 1978, 1983) or by a dipolar force-free magnetic field in two and half dimensions (Nakagawa et al. 1981; Wu et al. 1982). Sime et al. (1984), comparing the observed features of CMEs with numerical models, showed that those models are only able to qualitatively describe some of the observed characteristics.

Later models adopted as initial configurations either polytropic steady state streamers or quasi-steady state streamers with an ad hoc energy input (Steinolfson and Hundhausen, 1988, hereafter referred to as SH) and invoked either a thermal or a magnetic driving force as the perturbing agent responsible for CMEs' initiation. SH, for example, used three different pre-event atmospheres (hydrostatic state with dipole potential magnetic field; polytropic steady state streamer with dipole magnetic field; quasi-steady state heated streamer with dipole magnetic field) in their CME simulations. The structure of these pre-event coronae has been discussed by Steinolfson (1988), who suggested that using these modified initial atmospheres for CME simulation leads to a better agreement between models and observations. In fact, the models of mass ejections which were initiated at the base of the closed-field region of a dipole field in a hydrostatic atmosphere failed to simulate the most commonly observed features of loop-like CMEs because of the formation of a strong fast MHD shock. However, the simulations of a mass ejection in a polytropic corona with a streamer correctly reproduced two features (rarefaction between the legs and limited latitudinal leg motion), although the development of a fast shock compression front still yielded higher brightness at the loop top than in the legs, contrary to what is observed. SH prevented shock formation by introducing a volumetric heating term in their energy equation and simulating the CME energy source by an increased heating in a localized region within the closed field area, thus reproducing successfully most of the

looplike observed features. More recently, analogous results have been obtained by Guo et al. (1992), who used a similar polytropic streamer without heat source as pre-event atmosphere but with an emerging-flux type perturbation.

In this paper we use four different pre-event coronae, two similar to earlier cases and two with more realistically low densities outside the streamers, to further study the importance of the initial atmospheres in CME modeling. Section 2 illustrates the technique used to construct the pre-event atmospheres. The results of our simulations for pre-event coronae are illustrated in section 3. Their influence on the shapes and sizes of coronal mass ejections, as well as the modifications of the adjacent coronal hole regions at the time of CMEs events, are discussed in section 4. Concluding remarks are given in Section 5.

2. Numerical simulation method

The two-dimensional, fully implicit, continuous Eulerian scheme (FICE) in spherical coordinates (Wang et al., 1982) has been used to solve the ideal magnetohydrodynamic (MHD) equations (Wang et al., 1993) in the present study for both the pre-event coronae and CME simulations. The first version of FICE in cartesian coordinates was given by Hu and Wu (1984). One of the advantages of the FICE scheme is to incorporate the characteristic boundary conditions into the solutions process for the assurance of the self-consistency (Wu and Wang, 1987).

The computational and physical boundary conditions we adopt for the present numerical simulation are the following:

(i) Computational Domain and Grids.

In the latitude direction θ changes from $(-\Delta\theta/2)$ degrees (near the pole) to $(90^0 + \Delta\theta/2)$ degrees (near the equator). The spacing in θ-direction is $\Delta\theta = 4.5°$ so that there are 22 grid points in latitude; the first grid point is at $-2.25°$ and the last grid point is at $92.25°$. The pole ($\theta = 0°$) and the equator ($\theta = 90°$) are centered between grid points.

The spacing in the r-direction is $\Delta r_i = r_{i-1}(1 + \Delta\theta)$ and $r_i = R_\odot(1 + \Delta\theta)^{(i-1)}$. The computational domain in the radial direction includes 27 grid points and extends from

the solar surface to $7R_\odot$. With this grid selection. the two-dimensional grid cells have approximately square shape, which leads to a more evenly weighted numerical calculation.

(ii) Computational Boundary Conditions.

Side boundaries have been assumed to be symmetric and not crossed by any flow. At the outer boundary, the flow is generally supersonic and super-Alfvénic; hence, information from the outer boundary only propagates downstream. i.e., outside the region of interest. In other words, all eight radial characteristic directions at the outer boundary are positive. This implies that the boundary conditions at $7R_\odot$ can be specified arbitrarily. We choose the linear extrapolation method for this boundary.

(iii) Physical Boundary Conditions.

For the inner boundary, i.e. the physical boundary, the projected characteristics method has been used (Hu and Wu, 1984; Wu and Wang, 1987). In the two-dimensional problem, two of the six radial characteristic directions are negative (v_r is greater than zero but $(v_r - v_s)$ and $(v_r - v_f)$ are smaller than zero, where v_s and v_f are the slow and fast magneto-sonic speeds, respectively. v_r is the radial flow speed.); consequently, information from the region of interest propagates upstream to the boundary only along these two characteristic directions. In this case, four dependent variables at the lower boundary can be specified arbitrarily, and two must be calculated from the compatibility relations for every time step.

3. Pre-event coronal atmosphere

In order to carry out CME simulations, we first have to define the pre-event corona. In the present case, the four pre-event coronal atmospheres have been modeled, via a relaxation technique, by prescribing appropriate initial and boundary conditions to the set of ideal MHD equations.

In case 1, we solve the usual set of ideal MHD equations (the reader is referred to Wang et al., 1993, for a complete description of the equations), assuming constant density ($2.25 \times 10^8 cm^{-3}$) and temperature (1.8×10^6 K) at the solar surface, a polytropic

Parker-type solar wind solutions (with $\gamma = 1.05$) and a dipolar potential field configuration with the magnitude 1.67 gauss at the equator and 3.35 gauss at the pole on the solar surface. The steady state solutions for density, velocity and magnetic field, shown, respectively, in Figure 1a, 1b, 1c, are identical to those of Wang et al. (1993), and are similar to other published models (SH, 1988; Guo et al., 1992, Mikic et al. 1994, and Linker et al. 1992). These solutions adequately represent the streamer, but are unable to reproduce the characteristics of the adjacent coronal hole, as easily seen in the behavior of the density. Because of this deficiency, Noci et al. (1993) were unable to model the observed profile of the Lyman-α emission vs. height in the quiet corona using the case 1 model. The present study aims at modeling a pre-event coronal atmosphere capable of reproducing simultaneously both the streamer and the hole properties, which may lead to the better understanding of the modeling both the pre-event corona and CMEs. In order to construct such a streamer-hole solution, we adopted latitudinal dependent boundary conditions, assuming density **decreases** linearly from the equator ($1.43 \times 10^8 cm^{-3}$) to the pole($10^7 cm^{-3}$), and temperature **increases** linearly from the equator ($1.74 \times 10^6 K$) to the pole ($2.42 \times 10^6 K$). The magnitude of magnetic field is 1.36 gauss at the equator and 2.71 gauss at the pole on the solar surface. We understand that the temperature distribution is not realistic. The rationale for this choice lies in the need to provide the polar region with the additional energy required to produce a low-density, rapidly accelerating, plasma flow. The steady-state solutions obtained by using initial conditions as the aforementioned profiles of density and temperature, coupled with the Parker-type polytropic solar wind solution (with $\gamma = 1.05$) in a dipolar magnetic field configuration, are shown in Figure 2a, 2b , 2c. These give, respectively, the latitudinal variation of the density, of the radial component of the velocity and of the magnetic field at several representative heights in the solar corona. Obviously, this solution represents both a coronal hole at the pole and a streamer at the equator.

The choice of γ being 1.05 for the ideal MHD cases (case 1 and case 2) is based on the MHD solar wind flow solution. It assures the solar wind flow at the base is subsonic and

7

sub-Alfvenic and reaches supersonic and super-Alfvenic conditions at $7R_\odot$. But, the solar wind plasma is fully ionized plasma in which case γ should be 1.67. Hence, in cases 3 and 4 we adopt $\gamma = 1.67$ and modify the ideal MHD energy equation with a source term. To this end, we have added to the energy equation a volumetric heating term, similar to the one adopted by SH, given by

$$C e^{(-0.1(R-R_\odot)/R_\odot)}, \tag{1}$$

where C is an arbitrary constant whose value is dictated by the amount of the energy which is being added. Also like SH, we assume that the heat source term is independent of latitude and decays exponentially with altitude.

Figure 3 shows the results we obtain assuming $\gamma = 1.67$, and modifying the energy equation as previously described, and using the identical boundary and initial conditions as case 1. The results are qualitatively similar to case 1, and do not display any of the coronal hole properties because of the constant boundary conditions. However, the magnetic field configuration differs from that of case 1, as the closed field streamer region shows a sharp cusp reminiscent of observed configurations.

In case 4, we present (Figure 4) the results for latitudinal dependent boundary conditions identical to those of case 2; $\gamma = 1.67$, and a modified energy equation as in case 3. The latitudinal dependent boundary condition is used here to enable us to obtain streamer and hole simultaneously. Like case 3, the closed field streamer region shows a sharp cusp. In reference to case 2, we notice that the radial velocity of case 4 has increased appreciably because of the added volumetric energy source.

These four pre-event coronal models will be the initial states wherein CMEs will be simulated. Before going on to describe this part of our work, we would like to discuss further the pre-event atmospheres. We compute the total energy content of pre-event coronae by integrating four modes (thermal, kinetic, magnetic and gravitational) of energy over the computational domain. These results are given in Table I. These results show that, due to the introduction of additional heat source in the energy equation in cases 3 and 4 and

boundary conditions, these two pre-event coronae have a higher energy level than cases 1 and 2.

4. Coronal mass ejections in four model atmospheres

In order to examine the role of pre-event coronae in the modeling of coronal mass ejections (CMEs), we applied the same pressure and velocity perturbation at the inner boundary of the four model atmospheres, within the closed field region, i.e. within the interval $74.25° \leq \theta \leq 105.75°$. The pressure perturbation is described by a factor two increase both in the density and temperature; hence, pressure increases by a factor four with respect to its pre-event value. The velocity perturbation is set to zero at the edge of the closed field region (i.e. at $74.25°$) and varies linearly up to a maximum of 200 kms^{-1} near the equator (i.e. at $87.75 - 92.25°$). The velocity has also a linear temporal distribution between t = 0 to t = 200 s, defined in time steps of δt = 20 s and the pressure pulse is a step function. Both perturbations are maintained throughout the simulation. The total energy input resulting from this perturbation amounts to $\sim 6 \times 10^{24} erg$ km^{-1} and the total mass input is $\sim 6.8 \times 10^9 gkm^{-1}$. Taking into account that the latitudinal extent over which the perturbation is applied corresponds to seven grid points (or $3.8 \times 10^5 km$), the total energy input is $2.4 \times 10^{30} erg$ and the total mass input is $2.6 \times 10^{15} g$. These are comparable to the observed total energy and mass content of typical CMEs.

For each of the four pre-event coronae, we give the fractional density enhancement contours, the magnetic field configuration and the radial velocity at time = 3000 s and 9000 s, respectively which are summarized in the following.

Case 1 : Dipolar streamer with a polytropic gas, $\gamma = 1.05$.

In this case, the pre-event corona possesses the characteristics of a streamer, with no adjacent hole (i.e. no significant density contrast between the pole and equator). The density enhancement contours and magnetic field topology for the simulated coronal dynamical responses due to the pressure and velocity perturbation in this model atmosphere

are shown in Figure 5. These results are similar to those given by SH (1988), even though they used a perturbation given in terms of an energy input within a portion of the closed field region of the streamer together with modified energy equation, rather than a boundary perturbation and ideal energy equation as used in this study. Both results reproduce a number of observed characteristics of loop transient. including: (1) the high density region, in the shape of "legs", and, (2), the rarefraction region (low density) between the two legs. The propagation speed measured from the apex of the loop is ≈ 250 kms^{-1} which corresponds to a typical slow CME speed. This propagation speed is found to depend on the strength of the perturbation at the lower boundary.

Case 2 : Dipolar streamer and coronal hole with a polytropic gas, $\gamma =1.05$.

The simulated density enhancement contours and magnetic fields for this pre-event corona are shown in Figure 6. These results are basically similar to case 1 except that the loop system exhibits a larger latitudinal extension than case 1. This is due to the accompanying low-density coronal hole which has a larger fast-mode wave speed. From Figure 7 the initial β distribution in case 2 shows that when the density decreases from the equator to the pole the β values varies in latitude from $O[10]$ to $O[10^{-1}]$. In case 1, the density is almost uniform in latitude, thus the β value along latitude lines is also almost constant. By comparing the fast mode speeds in these two cases, the fast speed in case 2 along a latitude line is larger than that in case 1. Hence, the perturbation propagates more rapidly in latitude in case 2 than in case 1. The radial propagation speed for this case is ≈ 200 kms^{-1} which is lower than in Case 1, possibly because in this case loops show some latitudinal expansion.

Case 3 : Dipolar streamer in a heated atmosphere with $\gamma = 1.67$.

In this case, the density enhancement contours and magnetic field topology are completely different from those obtained in the two previous simulations, as shown in Figure 8. These results show two-stages of development. In the early stage (t $<$ 3000s), the simulation shows a low lying density and magnetic loop configuration (Figures 8a and 8b), while the magnetic field topology shows both loop shape and a magnetic island at

t=6000s (Figures 8c and 8d). In the later stage (t> 6000s), the magnetic island forms a distinct plasmoid shape which moves outward at a speed of 275 kms^{-1} with a loop shaped density enhancement and magnetic field lines extending outside the computational domain in Figures 8e and 8f. In this case the pre-event corona is in the highest energy level in comparison with the other three cases. From Figure 7c the β values at the equator near the solar surface within a small region are two order of magnitude larger than in the polar region. Thus, when velocity and pressure pulses were introduced the density in this region easily increases because the plasma is easily compressed. The field lines are pushed together to induce a pinch effect and to change the field topology into that believed to exist in magnetic clouds (Suess, 1988).

Case 4 : Dipolar streamer and coronal hole in a heated atmosphere with $\gamma = 1.67$.

The results for this case (shown in Figure 9) show that there are two bright legs (density enhancements) extending to the high corona, forming a spike-like structure with an overlying loop. According to the description of CME morphologies (Burkepile and St.Cyr, 1993), case 4 more like the mound : "the tops of mounds often have a well-defined, curved appearance similar to the frontal loop, but there is no obvious decrease in brightness behind the the leading edge". Unlike case 3, the magnetic field lines do not form a plasmoid. In this case the energy level initially is almost a factor two smaller than in case 3, but much larger than cases 1 and 2. Further, as shown in Figure 7d, the β distribution is similar to case 2 in which the value is smaller at the pole and larger at the equator, because the density is smaller at the pole and larger at the equator. But Figure 7 shows that the β values in case 4 (Fig. 7d) are much smaller than other three cases. This will lead to much easier propagation of the disturbances in the radial direction. Also the small β means that the magnetic field strength is strong, thus, the field lines are not easy to compress by latitudinal flow at the equatorial region to cause the formation of plasmoid as in case 3.

5. Discussions and concluding remarks

11

We have presented results from a numerical simulation of CMEs in four different pre-event coronae in which two cases possess both characteristics of streamer and hole, and have shown how pre-event coronal models affect CMEs simulations. In this section we discuss the new features of our work and compare it with previous numerical simulations of CMEs.

From these simulations, we obtain three distinct types of CMEs: (i) classical loop-like transients, (ii) plasmoid enveloped by a loop and (iii) spike-like legs in magnetic field configuration and mound shape of density enhancement. All these results are obtained using a standard perturbation with four different pre-event coronae. Now the question which needs to be answered is why ? Consider the energy content of the pre-event coronae, as given in Table I. This shows that case 3 has the highest energy content of all models. The reason for the variation of energy content is the different boundary conditions and additional energy being added in cases 3 and 4. Although we are unable, at this time, to give threshold values for the occurrence plasmoid, we surmise that a plasmoid-type CME occurs only when the pre-event corona has a sufficiantly high energy content. The middle range of energy content is responsible for mound-type CMEs, and the lowest range gives the classical loop-like CMEs. This conjecture coincides with observations reported by Burkepile and St.Cyr (1993), who ranked the morphologies of CMEs according to their relative frequency of appearance. showing that a loop-like transient is ranked first, followed by mound shape (in the fifth place) and blobs last (seventh place).

Steinolfson (1988) suggested that loop-like CMEs would originate in a pre-event atmosphere where shocks would not easily form. Simulations based on the present pre-event coronal models allow us to confirm this claim. In the four cases here the hightest density regions are behind the fast wave propagation lines. As shown, for instance, in Figure 9, the MHD fast-mode speed increases rapidly from the equator to the pole, along the meridional direction, as well as from the solar surface up to the open field regions, along the radial direction, thus preventing the formation of fast shocks.

From the beta distributions shown in figures 7 (initial β) and 10 (evolution of β), we can see why the present simulations show hardly any latitudinal displacement of the

bright legs in loop-like CMEs. The β at the site of the legs is very small ($\beta \approx 0.1$) in the pre-event atmospheres, so that the strong radial magnetic field prevents the propagation of mass motions in the latitudinal direction.

A comparison of the present results with previous work confirms the key role of the pre-event atmospheres in shaping the CME. We simulated loop-like transients in our cases 1, 2, and obtained results quite similar to those given by SH and Guo et al. (1992), but the perturbations are different in these different models. It looks as if our case 1 is analogous to SH and our case 2 mimics that of Guo et al. (1992).

We have already mentioned that a realistic simulation of both the streamer and coronal hole regions is achieved only in cases 2 and 4. The addition of an *ad hoc* heating term in the energy equation allowed us to obtain a more realistic cusp-shaped magnetic field configuration with a more realistic value of γ. The latitudinal dependent boundary conditions give a larger flow speed and a larger density depletion in polar, open field regions. It is worth noticing that, whenever we have the *ad hoc* heating term in the energy equation, the evolution shows that there is no exact steady-state solution such as in cases 1 and 2. But there is a quasi-steaty state with slow variation in comparison with the Alfven time. This may well correspond to recently acquired coronal images (Yohkoh) which show a continuously evolving solar corona.

In summary, these four pre-event coronae have resulted in three distinct shapes of CMEs. It could be said that these various shapes of transient are the results of pre-event coronal magnetic field configuration, physical characteristics (plasma thermodynamic properties) and the value of γ being used for a polytropic atmosphere.

All four model results have been shown to reproduce some commonly observed features of CMEs, as deduced from the large number of observations made with the white light coronagraphs on Skylab, P78-1, and SMM. A comparison with previous numerical models has clarified what is needed in order to simulate CMEs other than the classical looplike transients modeled in the past. Such studies are expected to help us gain more information about coronal properties in the vicinity of streamers and in coronal holes at the time CMEs

13

will be observed by UVCS (steady-state solution) and LASCO (time-dependent solution) on the SoHO mission.

Acknowledgements

References

Dryer, M., Wu., S. T., Steinolfson, R. S. and Wilson, R. M.: 1979, *Astrophys. J.*, **277**, 1059.

Gosling, J. T., Hildner, E., MacQueen, R. M., Munro, R. H., Poland, A. I., and Ross, C. L.: 1976, *Solar Phys.*, **48**, 389.

Guo, W. P., Wang, J. F., Liang, B. X. and Wu, S. T. : 1991, in Z. Svestka, B. V. Jackson and M. E. Machado (Eds), 'Eruptive Solar Flares', *IAU Symp.* **133**, 381.

Hildner, E.: 1977, in M. S. Shea *et al.* (eds.), *Studies of travelling interplanetary phenomena*, D. Reidel Publ. Co., Dordrecht, Holland.

Howard, R. A., Sheeley, N. R., Koomen, M. J. and Michels, D. J.: 1984, *Advanced Space Research*, **4**, 307.

Hundhausen, A. J.: 1977, in 'Coronal holes and high speed wind streams'. Colorado Associated University press.

Hundhausen. A. J., Burkepile. J. T. and St. Cyt, O. C.: 1994. *J. Geophys. Res.*, **99**, 6543.

Hu, Y. Q. and Wu, S. T.: 1984. *J. Comp. Phys.*, **55**, 33.

Illing, R. M. E.: 1984, *Astrophys. J.*, **280**, 399.

Mikic. Z. and Linker, J. A.: 1994. *Astrophys. J.*, **430**, 898.

Munro, R. H.: 1977, *Bull. Am. Astr. Soc.*, **9**, 371.

Munro, R. H., Gosling, J. T.. Hildner, E., MacQueen. R. M., Poland, A. I., and
Ross, C. L.: 1979, *Solar Phys.*, **61**, 201.

Nakagawa, Y. and Steinolfson. R. S.: 1976, *Astrophys. J.*, **207**, 296.

Nakagawa. Y., Wu, S. T. and Han. S. M.: 1978, *Astrophys. J.*, **219**, 314.

Nakagawa. Y., Wu, S. T. and Han, S. M.: 1978, *Astrophys. J.*, **244**, 331.

Noci, G., Poletto, G., Suess. S. T., Wang, A. H. and Wu, S. T. : 1993,
Solar phys., **147**, 55.

Rust, D. M., Hildner, E.. Dryer. M., Hansen, R. T., McClymont, A. N., McKenna-
Lawlor, S. M. P., McLean. D. J., Schmahl, E., Steinolfson, R. S., Tandberg -Hanssen
, E., Tousey, R., Webb, D.. and Wu, S. T.: 1980, in P. A. Sturrock (ed.), *Solar flares*,
Colorado Associated University Press.

Sheeley, N. R., Jr., Howard. R. A.. Koomen, M. J. and Michels, D. J.: 1980a, in M.
Dryer and E. Tandberg-Hanssen (eds.), 'Solar and Interplanetary Dynamics', *IAU
Symp.* **91**, 55

Sime, D. G., MacQueen, R. M.. and Hundhausen, A. J.: 1984, *J. Geophys. Res.*, **89**, 2113.

Steinolfson, R. S.: 1988, *J. Geophys. Res.*, **93**, 14261 .

Steinolfson, R. S. and Hundhausen, A. J.: 1988, *J. Geophys. Res.*, **93**, 14269.

Suess, S. T.: 1988, *J. Geophys. Res.*, **93**, 5437.

Tousey, R.: 1973, *Space Research* **12**, 713 (ed. by M. J. Rycroft and S. K. Runcorn).

Wang, A. H., Wu. S. T.. Suess. S. T.. and Poletto. G.: 1993, *Solar phys.*, **147**, 55.

Wang, S., Hu, Y. Q., and Wu. S. T.: 1982, *Scientifica Sinica*, **25**, 12.

Wu, S. T. and Wang, J. F. : 1987. Computer methods in applied mechanics and engineering , **64**, 267.

Wu, S. T., Wang, S., Dryer. M.. Poland, A. I., Sime, D. G., Wolfson, C. J., Orwig, L. E., and Maxwell, A.: 1983. *Solar Phy.*, **85**, 351.

Wu, S. T., Dryer, M., Nakagawa. Y. and Han, S. M.: 1978, *Astrophys. J.*, **219**, 324.

Wu, S. T., Hu, Y. Q., Wang. S.. Dryer, M. and Tandberg-Hanssen, E.: 1982, *Astrophys. Space Sci.*, **83**, 189.

Figure Captions

Figure 1. Latitudinal dependence of density and radial velocity at different heights (1a, 1b) and magnetic field lines (1c) for the pre-event corona of case 1.

Figure 2. Latitudinal dependence of density and radial velocity at different heights (2a, 2b) and magnetic field lines (2c) for the pre-event corona of case 2.

Figure 3. Latitudinal dependence of density and radial velocity at different heights (3a, 3b) and magnetic field lines (3c) for the pre-event corona of case 3.

Figure 4. Latitudinal dependence of density and radial velocity at different heights (4a, 4b) and magnetic field lines (4c) for the pre-event corona of case 4.

Figure 5. The evolution of density enhancement (a,c) and magnetic field (b,d) for case 1 at t=3000 s and t=9000 s after a standard perturbation was applied. The broken lines represent the fast wave front and the dotted lines represent the density depletion.

Figure 6. The evolution of density enhancement (a,c) and magnetic field (b,d) for case 2 at t=3000 s and t=9000 s after a standard perturbation was applied. The broken lines represent the fast wave front and the dotted lines represent the density depletion.

Figure 10. The two-dimensional distributions of plasma beta, β for pre- event coronae of case 1, 2, 3, and 4, respectively.

Figure 8. The evolution of magnetic field and density enhancement for case 3 at t=3000 s, t=9000 s after a standard perturbation was applied. The broken lines represent the fast wave front and the dotted lines represent the density depletion. It should be noted that the broken line does not appear at t = 9,000 s, because the fast waves have already propagated out of the computational domain.

Figure 9. The evolution of magnetic field and density enhancement for case 4 at t=3000 s and t=9000 s after a standard perturbation was applied. The broken lines represent the fast wave front and the dotted lines represent the density depletion. It should be noted that the broken line does not appear at t = 9,000 s, because the fast waves have already propagated out of the computational domain.

Figure 10. The two-dimensional distributions of plasma beta, β, for evolution states at 9000 second of case 1, 2, 3, and 4, respectively.

Energy Content of The
Pre-event Coronal Atmosphere

	Case 1	Case 2	Case 3	Case 4
E_M	6.00	4.56	13.79	9.55
E_K	0.39	0.66	2.57	1.60
E_T	4.26	4.05	8.35	4.20
E_G	8.17	7.45	13.60	6.59
Total $(10^{25} erg/km)$	18.78	16.72	38.31	21.94

Table I

Density Distribution (cm^{-3})

1.00R$_\odot$

1.35R$_\odot$

1.83R$_\odot$

2.47R$_\odot$

3.35R$_\odot$

4.53R$_\odot$

Polar Angle (degrees)

(a)

Radial Velocity (kms^{-1})

4.53R$_\odot$

3.35R$_\odot$

2.47R$_\odot$

1.83R$_\odot$

1.35R$_\odot$

1.00R$_\odot$

Polar Angle (degrees)

(b)

Magnetic Field Lines

7 6 5 4 3 2 1   1 2 3 4 5 6 7

(c)

Fig. 1

Fig. 2

Density Distribution (cm^{-3})

1.00R$_0$
1.35R$_0$
1.83R$_0$
2.47R$_0$
3.35R$_0$
4.53R$_0$

Polar Angle (degrees)

(a)

Radial Velocity (kms^{-1})

4.53R$_0$
3.35R$_0$
2.47R$_0$
1.83R$_0$
1.35R$_0$
1.00R$_0$

Polar Angle (degrees)

(b)

Magnetic Field Lines

7　6　5　4　3　2　1　　1　2　3　4　5　6　7

(c)

Fig. 4

Density Distribution (cm^{-3})

Radial Velocity (kms^{-1})
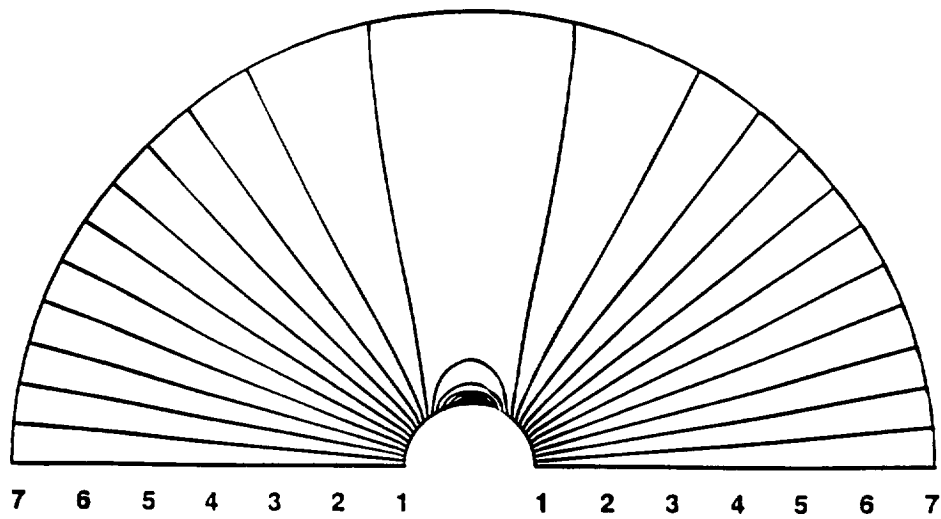
(a)

(b)

Magnetic Field Lines

(c)

Fig. 3

Density Distribution (d-d0)/d0

Magnetic Field Lines

t=3000s

(a)

(b)

t=9000s

(c)

(d)
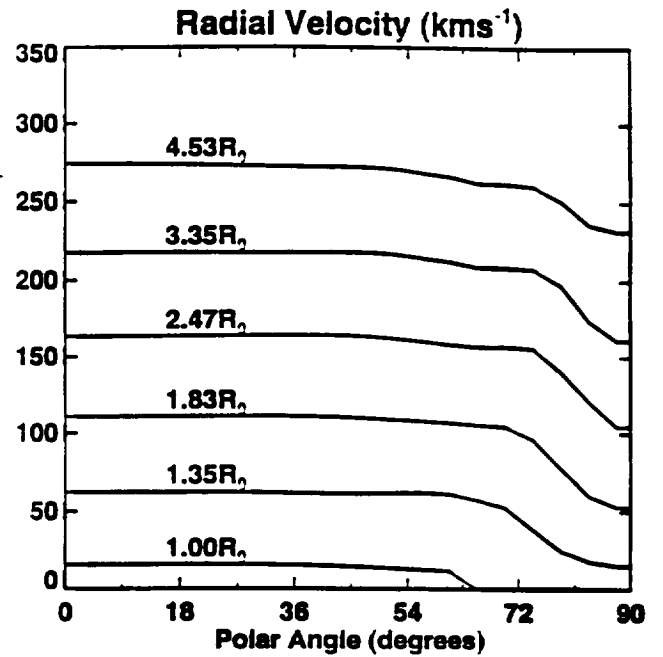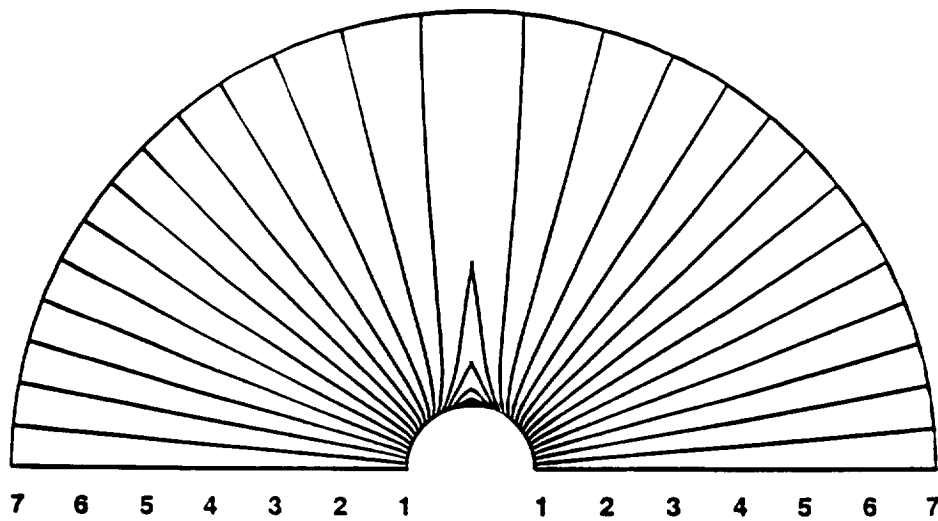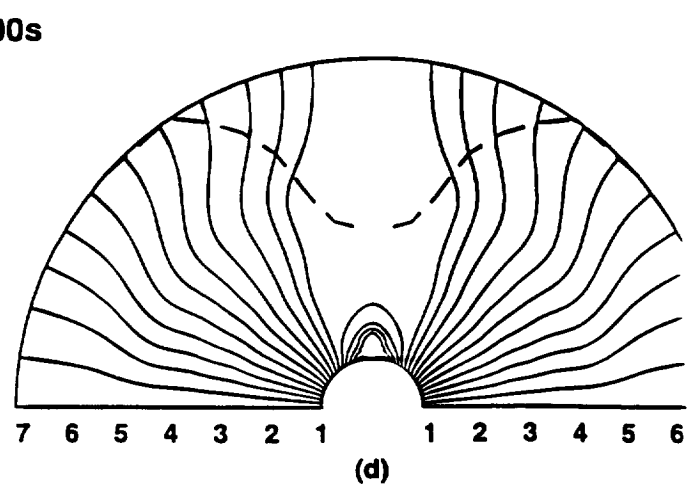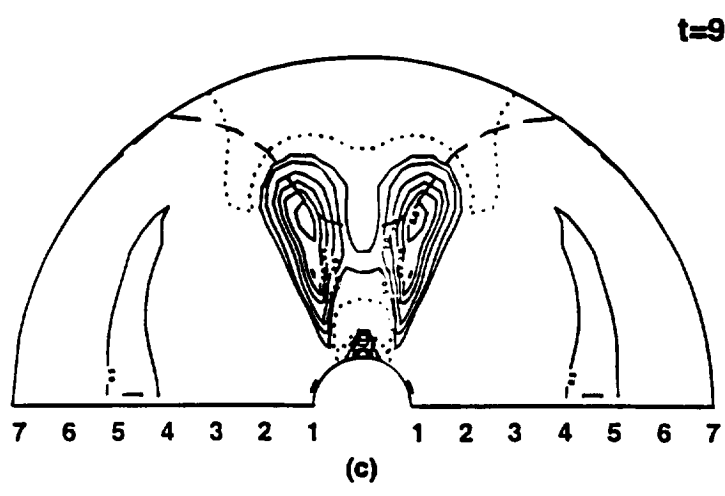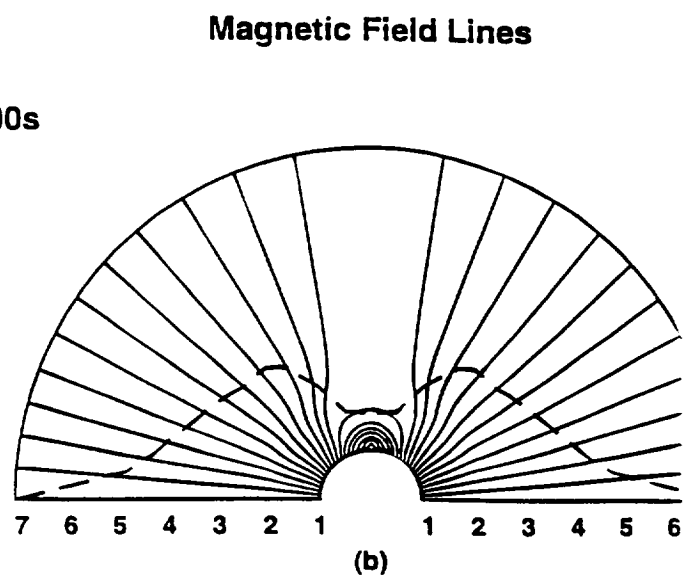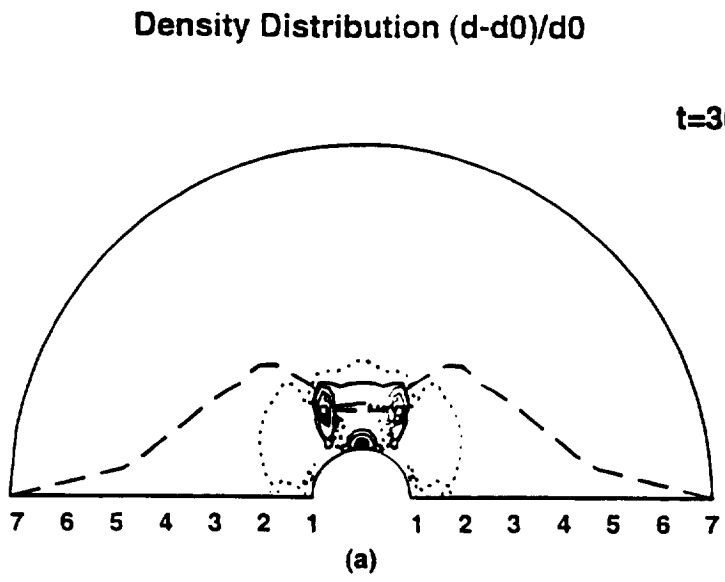
Fig. 5

Density Distribution (d-d0)/d0

Magnetic Field Lines
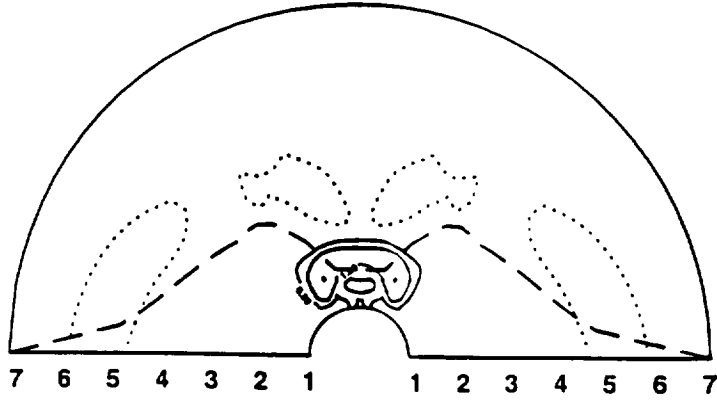
t=3000s

(a)
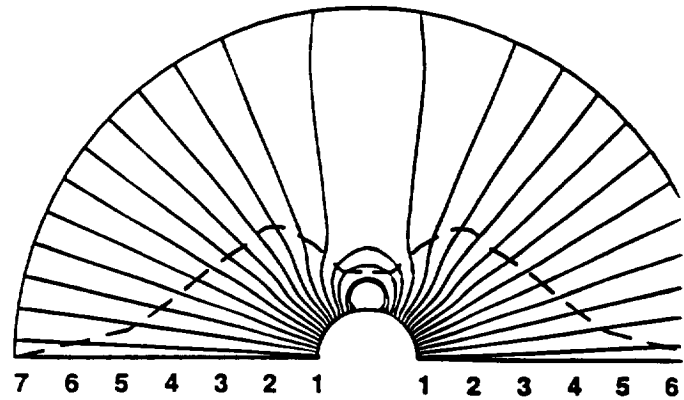
(b)
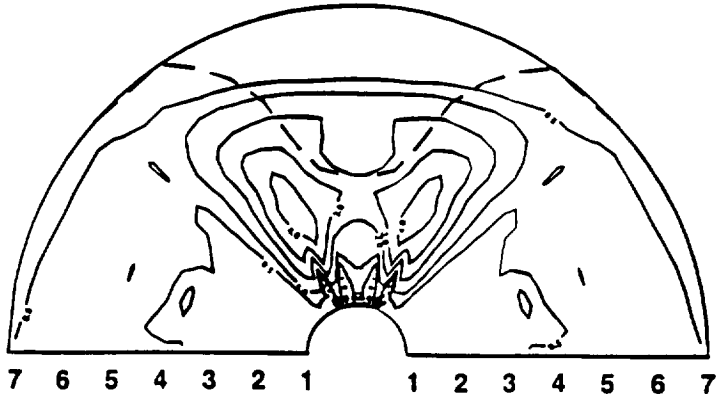
t=9000s

(c)
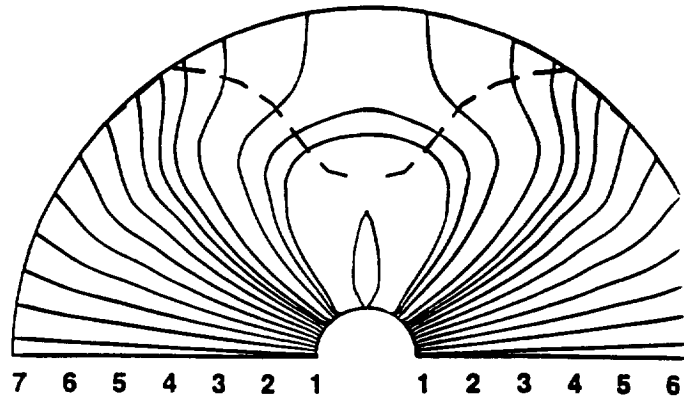
(d)

Fig. 6

Pre-event Plasma Beta Distribution
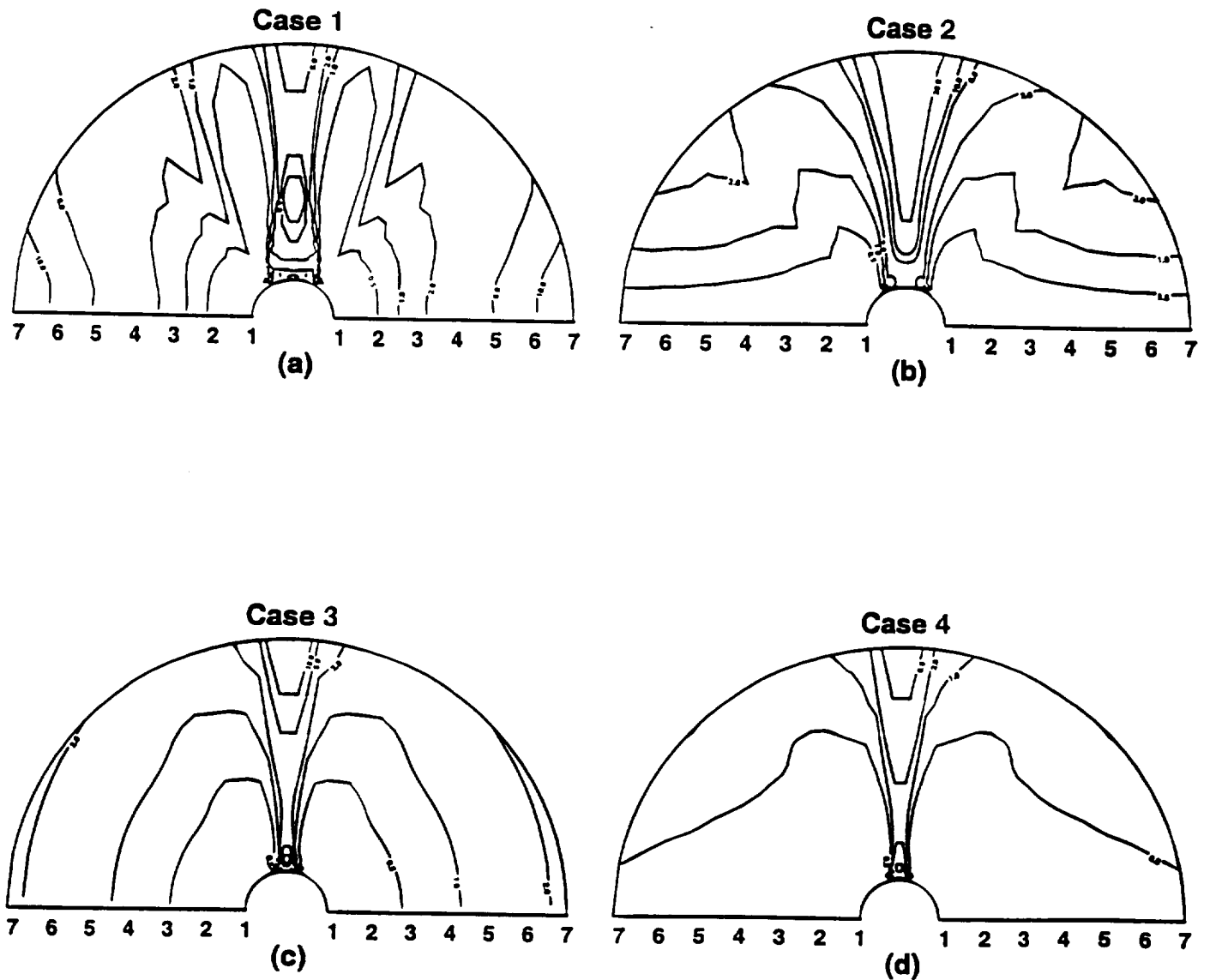
Case 1

(a)

Case 2

(b)

Case 3

(c)

Case 4

(d)

Fig. 7

Density Distribution (d-d0)/d0

Magnetic Field Lines

t=3000s

(a)

(b)

t=6000s

(c)

(d)

t=9000s

(e)

(f)

Fig. 8

Density Distribution (d-d0)/d0
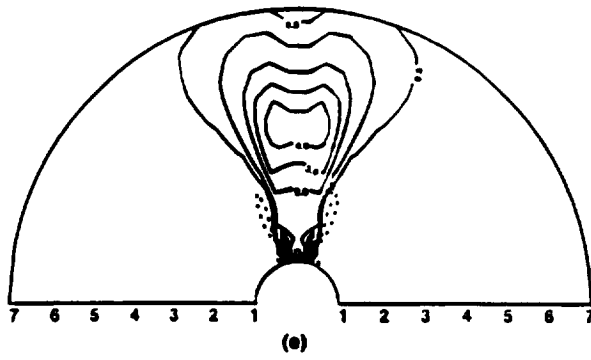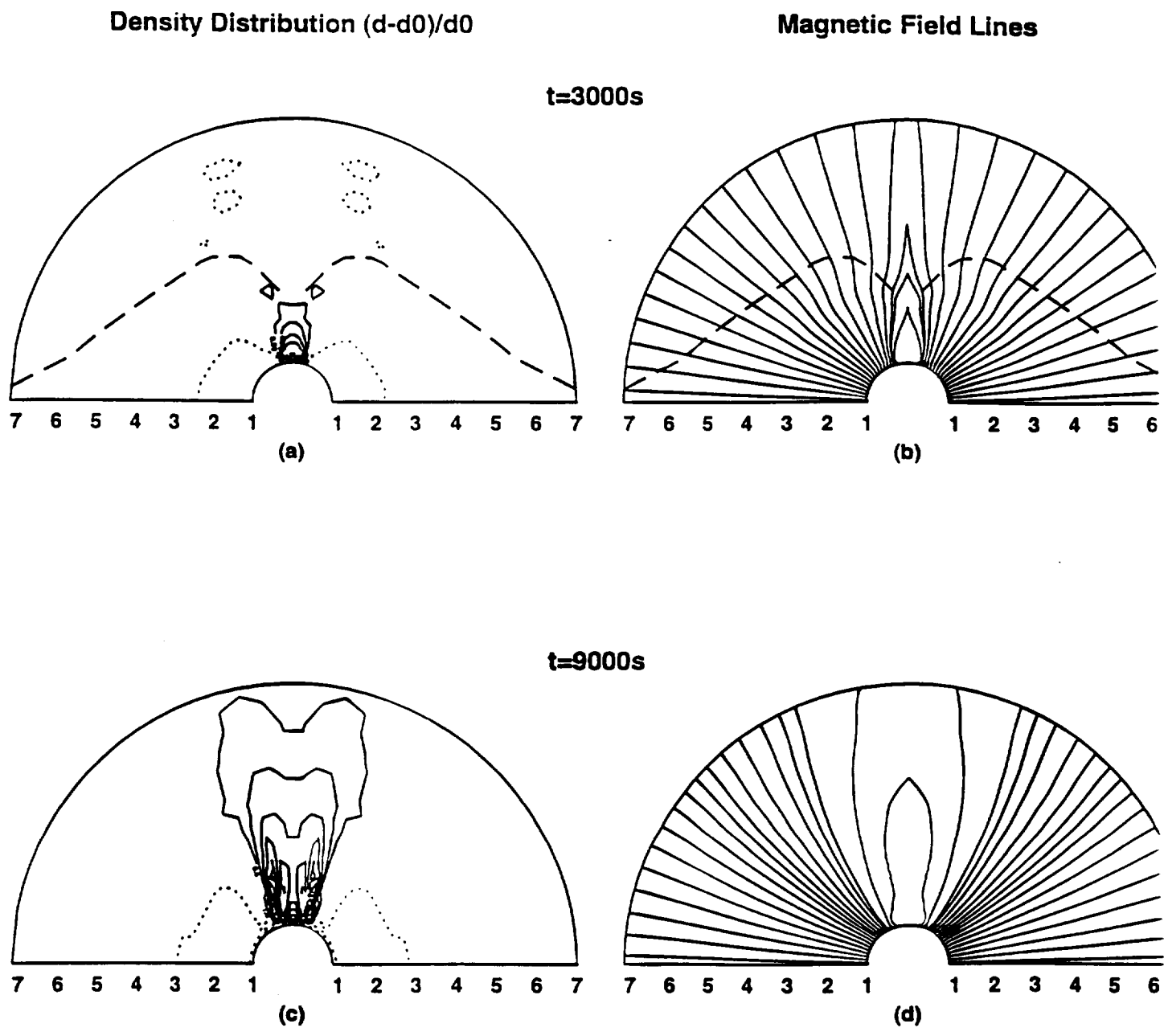
Magnetic Field Lines

t=3000s

(a)

(b)

t=9000s

(c)

(d)
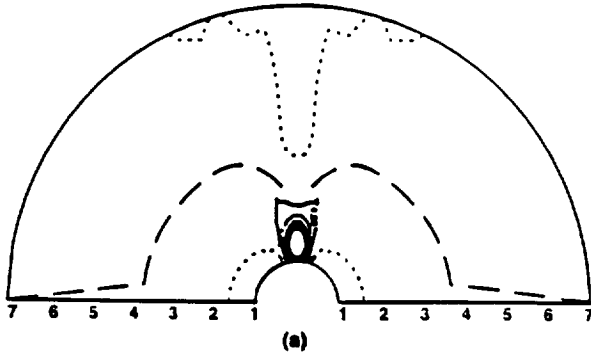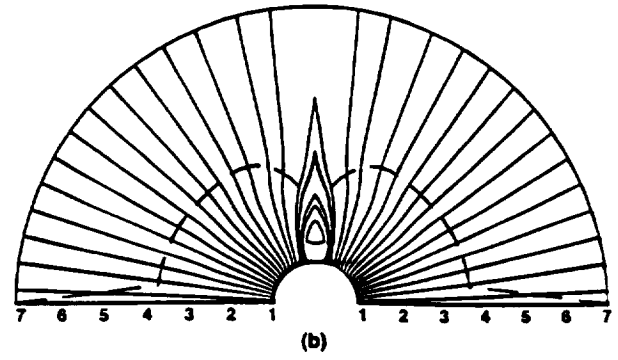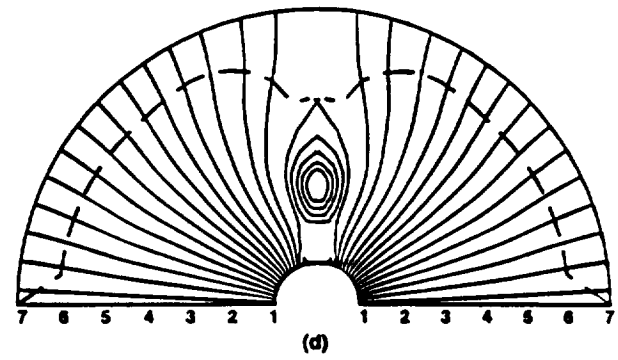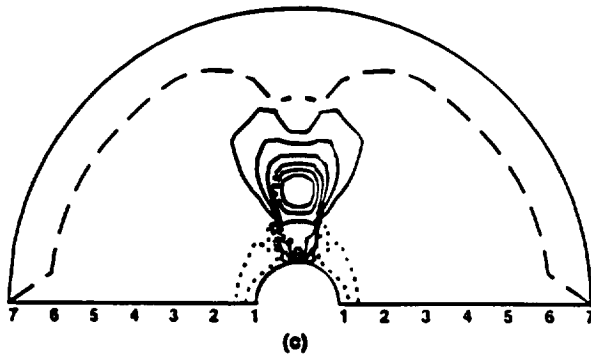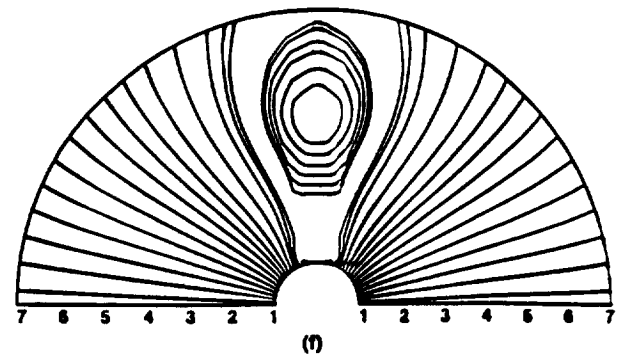
Fig. 9

Plasma Beta Distribution at 9000s

Fig. 10